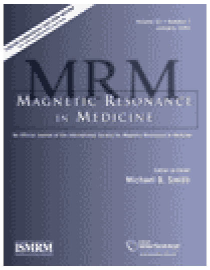

Mapping apparent eccentricity and residual orientation in the gray matter using angular double-PFG MRI

Journal:	*Magnetic Resonance in Medicine*
Manuscript ID:	Draft
Wiley - Manuscript type:	Full paper
Date Submitted by the Author:	n/a
Complete List of Authors:	Shemesh, Noam; Tel Aviv University, School of Chemistry Barazany, Daniel; Tel Aviv University, Department of Neurobiology Sadan, Ofer; Tel-Aviv Medical Center, Department of Neurology, Bar, Leah; Tel Aviv University, School of Mathematical Sciences Zur, Yuval; GE Healthcare Sochen, Nir; Tel Aviv University, School of Mathematical Sciences Barhum, Yael; Rabin Medical Center, Felsenstein Medical Research Center Offen, Daniel; Tel Aviv University, Human Molecular Genetics and Biochemistry Department; Rabin Medical Center, Felsenstein Medical Research Center Assaf, Yaniv; Tel Aviv University, Department of Neurobiology Cohen, Yoram; Tel Aviv University, School of Chemistry
Research Type:	Measurement techniques < Diffusion < Technique Development < Technical Research
Research Focus:	Anatomy < Brain < Neurological, Normal < Anatomy < Brain < Neurological

Mapping apparent eccentricity and residual orientation in the gray matter using angular double-PFG MRI

Noam Shemesh[1], Daniel Barazany[2], Ofer Sadan[3], Leah Bar[4], Yuval Zur[5], Yael Barhum[6], Nir Sochen[4], Daniel Offen[6], Yaniv Assaf[2] and Yoram Cohen[1*]

[1]School of Chemistry, The Raymond and Beverly Sackler Faculty of Exact Sciences, Tel Aviv University.

[2]Department of Neurobiology, The George S. Wise Faculty of Life Sciences, Tel Aviv University.

[3]Department of Neurology, Tel-Aviv Medical Center.

[4]School of Mathematical Sciences, The Raymond and Beverly Sackler Faculty of Exact Sciences, Tel Aviv University.

[5]GE Healthcare, Haifa.

[6]Human Molecular Genetics and Biochemistry Department, Sackler Faculty of Medicine, Tel Aviv University and Felsenstein Medical Research Center, Rabin Medical Center, Petah Tikva.

*Correspondence to:

Yoram Cohen,

School of Chemistry,

The Sackler Faculty of Exact Sciences,

Tel Aviv University, Ramat Aviv,

Tel Aviv 69978, Israel.

Tel: 972-3-6407232. Fax: 972-3-6407469

E-mail: ycohen@post.tau.ac.il

Number of words: ~5400 non inclusive of Figure Captions and References.

Running title: Novel sources of contrast in the rat brain by double-PFG MRI.

Abstract

Conventional diffusion MRI methods are mostly capable of portraying micro-architectural elements such as fiber orientation in white matter (WM) from detection of diffusion anisotropy, which arises from the coherent organization of anisotropic compartments. Double-Pulsed-Field-Gradient (d-PFG) MR methods are recently emerging as powerful means for obtaining novel microstructural information such as compartment shape and microscopic anisotropies even in scenarios where macroscopic organization is absent. Here, we apply angular double-Pulsed-Gradient-Spin-Echo (d-PGSE) MRI in the rat brain both ex-vivo and in-vivo for the first time. We show the theoretically predicted oscillations of the signal intensity at long mixing time (t_m) in the brain, but that many pixels exhibit unpredicted phases. We provide a theoretical explanation for these phases, showing that they are due to residual directors in randomly oriented media. We then developed an analysis scheme that yields maps of novel structural indices such as apparent eccentricity (aE) and residual phase (φ) that offered novel and exquisite contrasts in various areas of the rat gray matter. We conclude that owing to its enhanced sensitivity, d-PGSE MRI can become important in characterizing gray matter morphological features and pathologies in both basic and applied neurosciences.

Keywords: MRI, Magnetic Resonance imaging, gray matter, double-PFG,

Introduction

Central-nervous-system (CNS) tissues are characterized by intricate micro-architectural features which, through their organization and networking, give rise to the highly complex functions of the CNS (1). One of the most useful contrast mechanisms for studying CNS micro-architecture is based on the sensitization of the MRI signal to diffusion of endogenous water molecules since the diffusion process is highly affected by restricting boundaries. Indeed, in the early days of Diffusion Weighted Imaging (DWI), it was demonstrated that early ischemia can be detected (2) and that water diffusion appears anisotropic at least in white matter (3). Currently, Diffusion-Tensor-Imaging (DTI) (4) is widely used to study, *inter-alia*, structural connectivity and tractography of normal (5,6), developmental (7) and pathological (8) white matter tissues. Recently, diffusion MR was even used to study functional (9,10) aspects of the CNS. In all of these DTI applications, the diffusion anisotropy that is detected is in fact ensemble anisotropy (eA), arising from coherent organization of anisotropic compartments. In regions that are much less ordered, such as gray matter, conventional diffusion MRI methods yield exhibit low anisotropy (11-13), and thus relatively low contrast is obtained.

The double-Pulsed-Field-Gradient MR methodology (14-18) is an extension of conventional diffusion MR, applying *two* pairs of diffusion-sensitizing PFGs that are separated by a mixing time (t_m). Figure 1A shows an imaging sequence based on a double-Pulsed-Gradient-Spin-Echo (d-PGSE) sequence. One unique variant of d-PFG MR, namely the angular d-PFG MR methodology was first proposed theoretically by Mitra in 1995 (19). The angular experiment is performed by fixing the mixing time, diffusion periods, and gradient durations and amplitudes, and only varying the angle ψ between the gradients (Figure 1B). The initial theory (19) predicted that at low q-values, a bell-shaped signal intensity as function of ψ ($E(\psi)$) would emerge at short t_m, but strictly for restricted diffusion (as opposed to free, Gaussian or multi-Gaussian diffusion). These bell-shaped $E(\psi)$ dependencies were predicted to be proportional to the restricting length scale; therefore, angular d-PFG MR could potentially offer information on compartment size without requiring very strong gradients. Indeed, such bell-shaped E(ψ) dependencies were only very recently observed experimentally for the first time in MRI (20,21) as well as in d-PFG NMR spectroscopy in controlled organized systems (22-24).

Further recent progress in the theory and simulations of angular d-PFG MR suggested that it could uniquely report on microstructure even when there is no macroscopic ordering within the specimen (25-28), i.e. in systems where conventional diffusion MR yield little microstructural information owing to the low or zero FA. At long t_m, the E(ψ) plots of angular d-PFG MR were predicted to bear signatures for compartment shape anisotropy, thus offering a remarkable possibility to distinguish between compartments having different eccentricities (26). Indeed, these modulated E(ψ) curves at long t_m were recently observed for the first time in well controlled systems (29) as well as in various heterogeneous chemical and biological systems (30) and very recently, randomly oriented anisotropic compartments in isolated pig gray matter were detected for the first time (31). Additionally, ψ-independent E(ψ) plots were detected for spherical yeast cells (30). In all of the above cases, conventional diffusion MR methods only showed isotropic diffusion, thus demonstrating that unique microstructural information could be obtained from angular d-PFG MR.

Tensor approaches to angular d-PFG MR have been recently emerging that provide indices of microscopic anisotropy that are invariant to rotation (32,33) as well as the relationship of the signal decay with the displacement correlation tensor (34). Approaches aimed at increasing the extent of the angular dependencies by applying multiple concatenations have also been theoretically suggested recently (35,36) and a "phase-gymnastics" approach has been presented to more intuitively explain the signal differences at ψ=0° and 180° (37). Recently, Özarslan's theoretical findings were reproduced by extending the matrix formalism approach to angular d-PFG MR (38). Subsequently, an experimental study on a pig spinal cord phantom showed that d-PFG MRI experiments (dubbed double-wave-vector (DWV) experiments) could be performed on a clinical scanner (39).

Here, we perform angular double-PFG (d-PFG) MRI at long t_m for the first time on a rat brain both ex-vivo and in-vivo. We demonstrate for the first time that different modulated E(ψ) plots exist in different gray matter regions of the rat brain, but that in some regions, phases occur in the modulated E(ψ) plots. We show both intuitively and quantitatively that these phases can be attributed to residual orientation of anisotropic compartments in mostly randomly oriented media. A phenomenological quantitative approach towards characterizing novel indices such as apparent eccentricity (aE) and residual ordering phase (φ) is given, and novel maps based on these parameters are shown to offer novel sources of contrast within the gray matter. Finally, we show that similar findings can be obtained in-vivo in the rat brain using a conventional animal MRI scanner.

Materials and Methods

All animal experiments were approved by the University Committee of Animal Use for Research and Education. Male Wistar rats (N=5) weighing ~300 gr were intracardially perfused with 4% paraformaldehyde, and their brains were removed into a 4% paraformaldehyde solution. The ex-vivo rat brains were immersed in PBS overnight prior to the MRI experiments. The brains were placed in a 15mm glass tube filled with Fluorinert. A septum was used to seal the tube and Fluorinert was injected through the septum until no air bubbles were observed in the tube.

All MRI experiments were performed on a Bruker Biospec 7T scanner, equipped with a gradient system capable of producing up to 400 mT/m. The tube containing the brain was inserted such that the anterior-posterior axis of the brain was aligned along the z-direction. The orientation of the brain was carefully adjusted in the magnet such there was no angle difference between the two hemispheres. A volume coil was used for transmitting, while a quadurature coil placed directly above the tube was used as the receiving coil.

In the in-vivo measurement, anesthesia was induced using 4% isoflurane carried by a flow of 95% O_2, which was gradually reduced to ~1.5% isoflurane. The rat was placed on a heated bed, and its respiration rate was monitored. The same transmit/receive coils were used as for the ex-vivo setup.

A d-PGSE sequence with EPI readout was written in-house, allowing for completely free control of the variables $\mathbf{q_1}$, $\mathbf{q_2}$, Δ_1, Δ_2, δ_1, δ_2 and t_m. In all experiments in this study, we chose $|\mathbf{q_1}|=|\mathbf{q_2}|$, $\delta_1=\delta_2$ and $\Delta_1=\Delta_2$. The angular d-PGSE MRI experiments were performed in a similar fashion to the d-PFG spectroscopy experiments previously described (40). For a review on the d-PFG MR methodology, see Ref. (41). Briefly, Δs, δs and the q-value were fixed. $\mathbf{G_1}$ was set in the x-direction, and the orientation of $\mathbf{G_2}$ was varied in the X-Y plane along 13 ψ-values between 0º and 360º. The rat was aligned with its anterior-posterior axis pointing towards the x-direction (defined in Figure 1B). The X-Y plane is therefore defined as the axial plane, (the plane perpendicular to the slice shown in Figure 2 and parallel to the slice shown in Figure 7D-F).

Image Analysis. A code was written in Matlab® to analyze the images. The analysis included 5 steps. First, the 13 E(ψ) images were realigned and smoothed using a small Gaussian kernel of twice the voxel size. Second, a reference image was created according to $E_{ref}=\{E(\psi=0^\circ)+E(\psi=360^\circ)\}/2$ and each E(ψ) image was normalized to this reference image, i.e. $E(\psi)_{norm} = E(\psi)/E_{ref}$. Third, a mask was manually marked for the brain. Fourth, a Levenberg-Marquardt non-linear-least-squared routine was used to fit the data to the following equation:

$$E(\psi)_{norm} = 1 - aE*[\sin^2(\psi+\varphi)]+C \qquad \text{[Eq. 1]}$$

Where aE, φ and C were fitted parameters. The analysis was performed pixel-by-pixel. In the fifth and final step, maps of the fitted parameters were generated. For the parameter φ, a symmetrized colorcoded map was additionally created by assigning equal colors to the same positive and negative values of φ. In some cases, the absolute value of aE, |aE| was mapped.

DTI images were analyzed by extracting the diffusion tensor using the DiVa tool (http://diva-dti.sourceforge.net/) in Matlab®. The same mask was used for d-PGSE MRI and DTI images. The FA and color-coded FA maps were generated from the DTI data.

Experimental parameters for the MRI experiments. For the brains shown in Figures 6 and 8 (each coming from a different rat), the following parameters were used: t_m=15 ms, $\delta_1=\delta_2$=3.5 ms, $\Delta_1=\Delta_2$=20 ms, $|G_1|=|G_2|$=335.5 mT/m. resulting in a 2q value of 1000 cm^{-1}. The field of view (FOV) was 1.96x1.96 (cm^2) and the slice thickness was 800 μm. A matrix of 156x156 was chosen, resulting in an in-plane resolution of 125x125 (μm)^2. The repetition time/echo time (TR/TE) of the d-PGSE MRI experiments was 2800/65 ms (TE refers to the entire duration from the first RF pulse to the time of acquisition). The number of averages was 160, resulting in ~6.5 hours scan time per dataset.

For the brain shown in Figure 7A-C, the following parameters were used: t_m=15 ms $\delta_1=\delta_2$=3.8 ms, $\Delta_1=\Delta_2$=25 ms, $|G_1|=|G_2|$=340 mT/m. resulting in a 2q value of 1100 cm^{-1}. The field of view (FOV) was 1.8x1.8 (cm^2) and the slice thickness was 800 μm. A matrix of 128x128 was chosen, resulting in an in-plane resolution of 140x140 (μm)^2. The repetition time/echo time (TR/TE) was 2800/82 ms. The number of averages was 320, resulting in ~13 hours scan time. For the brain shown in Figure 7D-F, the same parameters as for the brain of Figures 7A-C were used except the orientation was axial and the field of view (FOV) was 2.28x2.8 (cm^2) and the matrix size was 182x182 resulting in the same in-plane resolution of 125x125 (μm)^2.

For the in-vivo rat brain, a relatively anterior slice was chosen since it contains much gray matter. The following parameters were used: t_m=15 ms $\delta_1=\delta_2$=3 ms, $\Delta_1=\Delta_2$=17 ms, $|G_1|=|G_2|$=360 mT/m. resulting in a 2q value of 920 cm^{-1}. The field of view (FOV) was 2.28x2.28 (cm^2) and the slice thickness was 800 μm. A matrix of 162x162 was chosen, resulting in an in-plane resolution of 140x140 (μm)^2. The TR/TE was 2000/62 ms. The number of averages was 72, resulting in ~2 hours scan time. A SE-DTI sequence with EPI readout was used with diffusion parameters that were set to be comparable to those outlined for d-PGSE MRI above, i.e. for DTI Δ was set to be equal to Δ_1 and δ was set to be equal to δ_1. In all cases, DTI was performed in 30 directions at a b-value of 1000 s/(mm)^2. The in-plane resolution and slice thickness were exactly as for the d-PGSE MRI sequence.

For histology, the brains were transferred to a solution of 30% sucrose in PBS for 48h at 4ºC, then transferred to PBS. The brains were then cryosectioned to ~10µnm thick slices. Sections were incubated in a blocking and permeabilization solution (5% normal goat serum, 1% bovine serum albumin and 0.5% Triton X100 in PBS) and incubated with a primary antibody overnight at 4ºC (mouse anti-TH (Sigma-Aldrich, 1:100). After washing with PBS, sections were incubated with a biotinilated secondary antibody (Gout anti-mouse, Invitrogen, Carlsbad, CA, 1:200) for one hour followed by 488-alexa conjugated streptavidin (1:500, Invetrogen).

Simulations. The general theory for diffusion-induced signal decay in double-PFG MR, first published in Refs (26,27) was implemented in Matlab®. For the simulations in this study, the $E(\psi)$ signal was computed using the expanded analytical solutions given in the above references. $E(\psi)_{norm}$ plots were obtained by dividing $E(\psi)$ with $E(\psi=0°)$. The following parameters were used for all simulations: In all cases, capped cylindrical compartments were considered, having a radius, r_0=4 µm and length, L=20 µm. The following double-PFG parameters were used: t_m=50 ms, $\delta_1=\delta_2$=1.5 ms, $\Delta_1=\Delta_2$=20 ms, $|G_1|=|G_2|$=782 mT/m resulting in a 2q value of 1000 cm^{-1}. $\mathbf{G_1}$ was set in the x-direction (φ_{Lab}=0º) and θ_{Lab}=90º, where φ_{Lab} and θ_{Lab} are the azimuthal angle and polar angle in lab coordinates, respectively, see Figure 1B) and the angle ψ was varied in the X-Y plane. The simulation considered three cases: (1) cylinders were completely randomly oriented along both φ_{Lab} and θ_{Lab}. (2) A residual coherent alignment was allowed for 30% of the cylinders along φ_{Lab}=45º, θ_{Lab}=90º while the rest of the cylinders were randomly oriented along both φ_{Lab} and θ_{Lab}. (3) A residual coherent alignment was allowed for 30% of the cylinders along φ_{Lab}=135º, θ_{Lab}=90º while the rest of the cylinders were randomly oriented along both φ_{Lab} and θ_{Lab}.

Results

Figure 2A shows the E(ψ) raw data images obtained from the d-PGSE MRI with EPI readout in the ex-vivo rat brain. The raw data clearly demonstrate that signal intensity variation occurs in many parts of the brain when ψ is varied. In several cortical regions, for example, the image intensity clearly diminished between ψ=0º and ψ=90º (arrow). Then, the image intensity increased between ψ=90º and ψ=180º, where the intensity appeared very similar to the intensity at ψ=0º. This E(ψ) oscillation then appears to be mirrored up to ψ=360º.

Figure 2B shows the normalized data, i.e. the $E(\psi)_{norm}$ images. Note that when the images are normalized, T2- and q-value-induced contrasts are eliminated, and the intensity variation between the images now arises solely from the angular dependence. As a consequence of normalization, the $E(\psi=0^{o})_{norm}$ appears uniform and is close to unity in all pixels. In the normalized data, the relative oscillations appear much more clearly compared to the raw data, and can be appreciated across the entire brain. In some cortical regions, the signal decreases by up to ~50% compared to its original E(ψ=0º) value, while in organized regions such as the corpus callosum, the signal increases by up to ~90% from its original value. Such strong variations are evident in most brain regions, and especially in gray matter.

Figure 3 shows a region of interest (ROI) analysis of six ROIs placed within the rat brain. Figure 3A shows an $E(\psi=90^{o})_{norm}$ image overlaid with three representative ROIs in each hemisphere. In the first ROI in the left hemisphere (black) a nearly perfectly symmetrical $E(\psi)_{norm}$ oscillation is observed (Figure 3B, black symbols). However, in an adjacent ROI (red), while the amplitude of the oscillation appears quite similar to the first ROI, the symmetry about ψ=180º is broken, and a phase shift of ~30º emerges (Figure 3B, red symbols). In the white matter (WM) of the left hemisphere (green ROI), the E(ψ) dependence appears as a mirror image of the oscillations in the cortex. In the right hemisphere, similar trends were observed (Figure 3C) with one noticeable difference: the phase shift in the red ROI appeared *opposite* compared to the phase shift in the left hemisphere (Figure 3C, red symbols). After inspecting the pixels in many slices and brains using different parameters, we find that the vast majority of pixels display similar oscillations as described above. We found that these oscillations can be robustly fitted to Eq. 1. To demonstrate the robustness of the analysis, we clustered the pixels to 24 clusters, which represent the signal oscillation in the entire brain. Figure 3D shows the experimental data (red) along with the fit to Eq. 1 (blue line) and the error of the fit (pink asterisks). It should be noted that the clustering was performed only for the purpose of this demonstration, while in all of the following results below, a pixel-by-pixel analysis was performed. Note that in many clusters, a phase is clearly observed in the $E(\psi)_{norm}$ data, and that Eq. 1 fits nicely to all the data (Figure 3D).

The emergence of the phase factor, φ, has not been predicted by the earlier published theory nor has it yet been observed experimentally. Figure 4 shows an intuitive rationalization of these observations by looking into the restrictions to the diffusion process that are encountered at each ψ-value. In an ideal coherently-placed compartment (Figure 4A), an inverted modulation can be understood by realizing that at ψ=0 and 180º, both diffusion weightings are applied along the main axis of the fibers where diffusion is free and independent of ψ. By contrast at ψ=90º and 270º, the second encoding probes highly restricted diffusion. Therefore, the signal attenuation should be much smaller compared to the cases of ψ=0º 180º, which will be manifested as an inverted modulation (Figure 4B, arrows correspond by their color to the gradient orientations in Figure 4A). If a tilt exists in the principal axis of the coherently organized compartment (Figure 4C), the situation is slightly more complicated. When ψ=0º, the normalized signal will have the value of unity (Figure 4D); however, as ψ is increased up to the tilt angle denoted 'α' in Figure 4C, the second diffusion weighting will probe less restriction, making the signal attenuation larger; therefore, we will see a gradual decrease in the $E(\psi)_{norm}$ up to $\psi=\alpha$ (Figure 4D, red arrow). The signal will increase between α and 90º+α where it will reach its maximum, owing to the larger restriction probed (purple arrow). Between 90º+α and 180º+α, the signal will decrease again reaching a minimum at ψ=180º+α (gray arrow). Note that at ψ=180º, the signal is intermediate (yellow arrow). An increase in restriction up to ψ=270º+α will then be exhibited (blue arrow). Finally the signal will decrease up to ψ=360º. Therefore, what is actually observed is a phase shift in the $E(\psi)_{norm}$ (depicted schematically in Figure 4D).

Figure 4E shows a distribution of cylinders that represent a discrete "random" distribution of anisotropic compartments. The individual $E(\psi)_{norm}$ curves for each representative orientation are shown in Figure 4F (small symbols, the colors of the cylinders correspond to the color of the symbols in the graphs). When summing the signal from the six cylindrical compartments shown in Figure 4F the modulated cos2ψ-like curve (thick black symbols) that is characteristic of compartment eccentricity that was predicted in (26) is reproduced, lending further credence to the phenomenological approach used here.

The above results in fact suggest that the emergence of a phase in the $E(\psi)$ oscillations could be due to residually oriented compartments within randomly oriented anisotropic compartments. This can be verified by using the analytical expressions presented in (26) to analyze such a scenario. Figure 5 shows the theoretical prediction for $E(\psi)$ in three different scenarios: cylinders that are completely randomly oriented (red), and cylinders that are residually coherently oriented at in the X-Y plane, i.e. at θ_{Lab}=90º with φ_{Lab}=45º axis (green) or φ_{Lab}=135º axis (blue). When all compartments are randomly oriented, the signal oscillation is completely symmetrical, while a phase emerges only when there is residual orientation. Note that here, the phase does not exactly correspond to the tilt angles, since only a residual orientation of 30% exists, while 70% of the compartments are randomly oriented.

After verifying that the data fit well to the phenomenological equation, the $E(\psi)_{norm}$ images of the rat brain were fit to Eq. 1. on a pixel-by-pixel basis. Figures 6A and 6B show maps based on apparent eccentricity, while Figures 6C and 6D shows maps based on the residual orientation, φ. Figure 6A shows that the aE values vary between ~-0.8 to 0.8 in the brain. The aE maps appear quite symmetrical when the two hemispheres are compared, and several remarkable features can be noted. First, when cortical gray matter is inspected from its superior part towards the inferior part, a contrast arises, showing between five and six "layers" in the aE maps. Furthermore, a distinct contrast emerges between the areas of the most medial part of the gray matter, which has negative aE (thus appearing blue), and the more lateral gray matter area, which has a positive aE. The gray matter of the striatum also shows non-uniformity in aE contrast; furthermore, the striatal gray matter has different aE compared with cortical gray matter (Figure 6A). Note that in these aE images, the white matter (for example the corpus callosum) does not appear homogeneous, but shows a variation in the sign of aE along the white matter: in the regions where the corpus callosum is more aligned in the medial-lateral direction, the aE appears negative, while where it is aligned in a more superior-inferior direction, the aE is positive. Figure 6B shows a map of absolute-valued aE, |aE|. Here, the white matter of the corpus callosum appears more uniform; however, in the cortical gray matter, the layering is still clearly evident, and the contrast within the striatum remains robust. In some cases, the aE values for cortex and white matter are similar in magnitude.

Figure 6C shows the map of the residual orientation, φ. Remarkably, these images reveal strong contrast, especially in gray matter regions of the cortex. Looking from the most medial part laterally in the cortex, the φ parameter creates a contrast that appears as "bands" of varying φ-values across the cortex. Notably, the variation in the values of φ in one hemisphere is mirrored in the second hemisphere, but with *opposite* signs of φ; this indeed reflects the opposite residual orientations of compartments in the gray matter between the two hemispheres. To verify that the φ-values are indeed symmetrical across the brain, the colorbar was symmetrized with respect to 0; indeed, a highly symmetrical image of φ_{sym} is then obtained (Figure 6D). Note also the strong contrast that appears in the gray matter of the striatum in both φ and φ_{sym} maps, where the contrasts are opposite in sign in φ and highly symmetrical in φ_{sym}.

To show that these phenomena are general and robust, we performed the same experiments in several rat brains and in different brain slices, and with different imaging gradient orientations. The results are summarized in Figure 7. Figures 7A-C show the aE, φ and φ_{sym} of a more posterior coronal slice (compared to Figure 6) and Figures 7D-F show an axial slice from a different rat brain. All of the trends that were outlined above appear robust across the different brains and regardless of the direction of the imaging gradients. Note the high medial-to-lateral symmetry in the aE and the φ_{sym} maps. In the more posterior slice, layers of the hippocampus are highly delineated in the aE maps (Figure 7A-C).

Figure 8 shows aE, φ and φ_{sym} maps of yet another rat brain adjacent to the corresponding anatomical atlas slice (42). In the cortical gray matter, a strong contrast showing cortical layers is apparent (Figure 8A). The φ and φ_{sym} maps show many different bands of φ in the gray matter (Figures 8B and 8C). The corresponding anatomical atlas (Figure 8D) shows fewer regions within the cortical gray matter compared to the φ-contrast; However, it should be noted that this could be due to the partial volume effect of more posterior parts of the brain in the MRI image, which cannot be viewed in the atlas.

Several interesting spatial patterns arise in these images. Note the contrast marked with arrows in Figure 8C, which appears highly symmetrical in the contralateral hemisphere – this contrast is clearly not present in the anatomical atlas. Note that a similar spatial pattern to that delineated with the arrows in Figure 8C can also be observed in Figure 6D, in a completely different brain and in a more posterior slice.

Figure 8E shows an enlargement of the box highlighted in Figure 8B. Note that in the cortex, a contrast arises from left to right in the form of φ-values varying from negative to positive values. Histological staining for TH^+ neurons (Figure 8F,G) shows a "diluted" view of the neuronal cytoplasm. Some residual ordering within the stained region can be observed, demonstrating that the orientation varies in its direction across the section. Inspecting the images with higher magnification reveals the slight ordering more clearly (Figure 8G).

Figure 9 shows in-vivo d-PGSE MRI images obtained from a rat brain along with DTI experiments. The FA maps obtained from DTI (Figure 9A) showed high fractional anisotropy in the white matter regions, while in the gray matter, very little contrast and low FA values were observed. However, a contrast resembling cortical layering can be viewed in the gray matter in-vivo from aE maps (Figure 9B) obtained from the d-PGSE MRI, although some layering is also evident in the DTI images (Figure 9A). Plotting the intensity of each parameter across a line in the cortex (Figure 9C) reveals some similarities between the two parameters, although in the more medial parts, the aE maps seem to show more contrast.

The φ_{sym} maps of the rat brain in-vivo show the same trends as observed ex-vivo (Figure 9E). Note that many bands of varying values of φ can be observed in the cortex, showing remarkable contrast and providing contrast based on residual orientation of compartments within the gray matter region. The color coded DTI image (Figure 9D) seem to show much less contrast in the gray matter; indeed, when the intensity variations are examined across a representative row in the cortex, the variations in φ_{sym} show markedly different patterns as compared to the DTI images, clearly revealing that a novel contrast arises in the cortex (Figure 9F). Note also that the φ_{sym} maps show contrast within the gray matter of the striatum, that cannot be observed from neither FA maps or color coded FA maps.

Discussion

Single-PFG MR methods are capable of detecting eA in coherently organized compartments, which make them very useful for characterizing white matter in the CNS. Since angular d-PFG MR can detect additional parameters such as microscopic anisotropy (μA) and compartment shape anisotropy (csA), it is emerging as a means for providing novel microstructural information in more heterogeneous scenarios (30,31,41). Previous angular d-PFG MRI experimental studies involved sequences such as a multiple-spin echo sequence (20) that was performed on phantoms and spinal cord, a double-Stimulated-Echo (d-STE) MRI sequence with EPI readout that was performed at 17.6T and focused on the white matter of the ex-vivo rat spinal cord at short t_m (21), and a d-PFG-filtered MRI sequence that was performed on a glass capillary array phantom (43). In this study, for the first time, we introduced a d-PGSE MRI sequence with EPI readout, that was performed at long t_m in the rat brain both ex-vivo and in-vivo, on a conventional 7T scanner, and investigated the angular dependence and the information that can be obtained from it especially in gray matter tissues.

The gray matter is a highly heterogeneous tissue, comprised mostly of neuronal cell soma, axons, dendrites, as well as neuroglia and connective tissue. In the rodent, cortical layering of the gray matter is evident under histology in the superior-inferior aspect of the brain (44), and different cytoarchitectonic features such as varying cell densities can be observed in the medial-lateral aspect (45). Extremely high-resolution MRI images show cortical layering even T2 weighted images (46), and injection of contrast agents such as $MnCl_2$ also seems to generate contrast within the cortical layers of the rat neocortex (47).

Owing to the high microstructural heterogeneity of the gray matter, low FA values are detected in DTI studies of the rodent gray matter although in some cases, color-coded images do show some contrast in medial-lateral directions, as well as some degree of cortical layering (11,12). While high FA values in white matter correspond to the eA present, the low FA values in gray matter are more difficult to interpret. Therefore, methods such as angular d-PFG MRI that report on other microstructural parameters such as μA, that reflects compartment size and csA, which reflects the compartment eccentricity, may afford new sources of contrast in the gray matter. Indeed, previous studies showed that very accurate compartment sizes can be quantitatively extracted using this methodology in coherently organized (22) as well as randomly oriented pores (29); However, the gray matter tissue is highly complex, and each of the gray matter components (cell bodies, axons, etc.) may be characterized by its size distribution, its shape, as well as its volume fraction. Furthermore, each component may exhibit further compartmentation into, for example, intra- and extra-cellular spaces, which may have their own unique size and shape distributions. Another factor is exchange between these compartments and between the different components. A general model that accurately takes into account the fractional contribution of such microstructural elements and especially the size and shape distributions of intra- and extra-cellular compartments is not yet available; we therefore did not attempt to fit the d-PGSE MRI data to the elaborate theory that was so far published (25-27,32,33), or attempt to extract absolute information, such as axon size or eccentricity; indeed, such quantitative description would require numerous assumptions on the μA, csA, and eA of each of the microstructural elements that were mentioned above. Rather, we attempted to fit the data using a phenomenological equation that would fit to the vast majority of pixels in the brain, and indeed we found that Eq. [1] is adequate. Furthermore, Eq. 1 yields new microstructural parameters such as the apparent eccentricity and the residual orientation (φ) and the values of aE and φ, were found to be consistent and robust across brains, slices, and imaging planes. Moreover, these parameters seem to provide new sources of contrast for the rat brain, especially in the gray matter; an added value of these parameters is that they arise solely from restricted diffusion.

One of the major findings of this study is that a phase emerges in the signal oscillation in numerous gray matter regions. This is the first study to report this feature of E(ψ) in angular d-PFG MR; both an intuitive and a quantitative explanation for this phenomenon suggest that it arises from residual orientation of coherently organized compartments in otherwise disordered media. The φ maps reveal a striking new source of contrast in the brain, showing very strong variance of compartments across the cortex. Assigning the residually oriented compartments in the gray matter to a biological component will not be straightforward and will merit further future studies. Indeed, even in white matter, where compartments are coherently organized and fully myelinated, the source of diffusion anisotropy in DTI remains highly debated (48) and many mechanisms may contribute to the ADC values in DWI (49,50).

While the potential of d-PGSE MRI to uncover underlying microarchitectural features in the brain in-vivo seems very promising, there also exist some limitations. First, angular d-PGSE MRI is not invariant to rotation in cases where residual orientation exists, and therefore, the aE and φ maps are very strongly dependent on the plane of acquisition, i.e. the plane where the angle ψ is varied. Another limitation that arises from this rotational dependence is that the φ maps need to be inspected with close correlation to the aE maps, since φ can have the same value when aE<0 or aE>0. Further studies are needed to develop methods that will efficiently measure indices that are invariant to rotations and compare them to what is obtained from different planes of acquisition in d-PGSE MRI. Indeed preliminary theoretical studies in this direction are already emerging (32,33). Meanwhile, the experiment can be conducted in the X-Y plane simply by either ensuring that the brains are perfectly aligned or by carefully rotating the plane of acquisition with the tilt angle of the brain.

Another limitation is that the gradients used in this study were stronger (~360 mT/m) than those found in the clinical scanners (up to 80 mT/m). To achieve the same q-value used in this study using the maximum clinically available gradients, one would need to prolong the diffusion gradient duration by a factor of ~4.5. Although it was predicted that prolonging the diffusion gradient duration would reduce the amplitude of the oscillations (26,28), it remains to be seen how d-PGSE MRI performs in the clinic.

Conclusions

In conclusion, d-PGSE MRI was performed at long t_m for the first time in the rat brain both ex-vivo and in-vivo. We presented a simple and robust analysis method for the data, and showed that the resulting maps of novel parameters such as apparent eccentricity (aE) and residual phase (φ) yield novel contrasts in the gray matter both ex-vivo and in-vivo. This promising new source of contrast in MRI may become important in studying normal, developmental and neuropathological processes in the CNS and especially in the gray matter in both basic and applied sciences.

Acknowledgments

N.S, D.B., Y.A. and Y.C. were partially supported by the CONNECT consortium administered by the European Commission under framework package 7. The MRI scanner used in this study was purchased with grants from the Israel Science Foundation and the Raymond and Beverly Sackler Center for Biophysics, Tel Aviv University, and is operated by the Alfredo Federico Strauss Center for Computational Neuro-Imaging, Tel Aviv University. N.S. would like to thank the Clore Scholars Program for a scholarship.

References

1. Varela F, Lachaux JP, Rodriguez E, and Martinerie J. The brainweb: Phase synchronization and large-scale integration. Nat Rev Neurosci 2001;2:229-239.

2. Moseley ME, Cohen Y, Mintorovitch J, Chileuitt L, Shimizu H, Kucharczyk J, Wendland MF, and Weinstein PR. Early detection of regional cerebral-ischemia in cats - comparison of diffusion-weighted and T2-weighted MRI and spectroscopy. Magn Reson Med 1990;14:330-346.

3. Moseley ME, Cohen Y, Kucharczyk J, Mintorovitch J, Asgari HS, Wendland MF, Tsuruda J, and Norman D. Diffusion weighted MR imaging of anisotropic water diffusion in cat cnetral-nervous-system. Radiology 1990;176:439-445.

4. Basser PJ, Mattiello J, and Lebihan D. Diffusion tensor spectroscopy and imaging. Biophys J 1994;66:259-267.

5. Izhikevich EM and Edelman GM. Large-scale model of mammalian thalamocortical systems. Proc Nat Acad Sci USA 2008;105:3593-3598.

6. Behrens TEJ, Johansen-Berg H, Woolrich MW, Smith SM, Wheeler-Kingshott CAM, Boulby PA, Barker GJ, Sillery EL, Sheehan K, Ciccarelli O, Thompson AJ, Brady JM, and Matthews PM. Non-invasive mapping of connections between human thalamus and cortex using diffusion imaging. Nat Neurosci 2003;6:750-757.

7. Hagmann P, Sporns O, Madan N, Cammoun L, Pienaar R, Wedeen VJ, Meuli R, Thiran JP, and Grant PE. White matter maturation reshapes structural connectivity in the late developing human brain. Proc Nat Acad Sci USA 2010;107:19067-19072.

8. Horsfield MA and Jones DK. Applications of diffusion-weighted and diffusion tensor MRI to white matter diseases - a review. NMR Biomed 2002;15:570-577.

9. Le Bihan D. Looking into the functional architecture of the brain with diffusion MRI. Nat Rev Neurosci 2003;4:469-480.

10. Le Bihan D, Urayama S, Aso T, Hanakawa T, and Fukuyama H. Direct and fast detection of neuronal activation in the human brain with diffusion MRI. Proc Nat Acad Sci USA 2006;103:8263-8268.

11. Huang H, Yamamoto A, Hossain MA, Younes L, and Mori S. Quantitative cortical mapping of fractional anisotropy in developing rat brains. J Neurosci 2008;28:1427-1433.

12. Hui ES, Cheung MM, Qi LQ, and Wu EX. Towards better MR characterization of neural tissues using directional diffusion kurtosis analysis. Neuroimage 2008;42:122-134.

13. Kroenke CD, Van Essen DC, Inder TE, Rees S, Bretthorst GL, and Neil JJ. Microstructural changes of the baboon cerebral cortex during gestational development reflected in magnetic resonance imaging diffusion anisotropy. J Neurosci 2007;27:12506-12515.

14. Cory DG, Garroway AN, and Miller JB. Applications of spin transport as a probe of local geometry. Polymer Preprints 1990;31:149-150.

15. Cheng Y and Cory DG. Multiple scattering by NMR. J Am Chem Soc 1999;121:7935-7936.

16. Callaghan PT and Komlosh ME. Locally anisotropic motion in a macroscopically isotropic system: displacement correlations measured using double pulsed gradient spin-echo NMR. Magn Reson Chem 2002;40:S15-S19.

17. Komlosh ME, Horkay F, Freldlin RZ, Nevo U, Assaf Y, and Basser PJ. Detection of microscopic anisotropy in gray matter and in a novel tissue phantom using double Pulsed Gradient Spin Echo MR. J Magn Reson 2007;189:38-45.

18. Komlosh ME, Lizak MJ, Horkay F, Freidlin RZ, and Basser PJ. Observation of microscopic diffusion anisotropy in the spinal cord using double-pulsed gradient spin echo MRI. Magn Reson Med 2008;59:803-809.

19. Mitra PP. Multiple Wave-Vector Extensions of the Nmr Pulsed-Field-Gradient Spin-Echo Diffusion Measurement. Phys Rev B 1995;51:15074-15078.

20. Koch MA and Finsterbusch J. Compartment size estimation with double wave vector diffusion-weighted Imaging. Magn Reson Med 2008;60:90-101.

21. Weber T, Ziener CH, Kampf T, Herold V, Bauer WR, and Jakob PM. Measurement of apparent cell radii using a multiple wave vector diffusion experiment. Magn Reson Med 2009;61:1001-1006.

22. Shemesh N, Özarslan E, Basser PJ, and Cohen Y. Measuring small compartmental dimensions with low-q angular double-PGSE NMR: The effect of experimental parameters on signal decay. J Magn Reson 2009;198:15-23.

23. Shemesh N, Özarslan E, Bar-Shir A, Basser PJ, and Cohen Y. Observation of restricted diffusion in the presence of a free diffusion compartment: single- and double-PFG experiments. J Magn Reson 2009;200:214-225.

24. Shemesh N, Özarslan E, Basser PJ, and Cohen Y. Detecting diffusion-diffraction patterns in size distribution phantoms using double-pulsed field gradient (d-PFG) NMR: Theory and experiments. J Chem Phys 2010;132:034703.

25. Özarslan E and Basser PJ. Microscopic anisotropy revealed by NMR double pulsed field gradient experiments with arbitrary timing parameters. J Chem Phys 2008;128:154511.

26. Özarslan E. Compartment shape anisotropy (CSA) revealed by double pulsed field gradient MR. J Magn Reson 2009;199:56-67.

27. Özarslan E, Shemesh N, and Basser PJ. A general framework to quantify the effect of restricted diffusion on the NMR signal with applications to double pulsed field gradient NMR experiments. J Chem Phys 2009;130:104702.

28. Koch MA and Finsterbusch J. Numerical simulation of double-wave vector experiments investigating diffusion in randomly oriented ellipsoidal pores. Magn Reson Med 2009;62:247-254.

29. Shemesh N, Özarslan E, Adiri T., Basser PJ, and Cohen Y. Noninvasive bipolar double-pulsed-field-gradient NMR reveals signatures for pore size and shape in randomly oriented, polydisperse, inhomogeneous porous media. J Chem Phys 2010;133:044705.

30. Shemesh N, Adiri T., and Cohen Y. Probing microscopic architecture of opaque heterogeneous systems using double-Pulsed-Field-Gradient NMR. J Am Chem Soc 2011;133:6028-6035.

31. Shemesh N and Cohen Y. Microscopic and compartment shape anisotropies in gray and white matter revealed by angular bipolar double-PFG MR. Magn Reson Med 2011;65:1216-1227.

32. Finsterbusch J and Koch MA. A tensor approach to double wave vector diffusion-weighting experiments on restricted diffusion. J Magn Reson 2008;195:23-32.

33. Lawrenz M, Koch MA, and Finsterbusch J. A tensor model and measures of microscopic anisotropy for double-wave-vector diffusion-weighting experiments with long mixing times. J Magn Reson 2009.

34. Jespersen SN and Buhl N. The displacement correlation tensor: Microstructure, ensemble anisotropy and curving fibers. J Magn Reson 2011;208:34-43.

35. Finsterbusch J. Extension of the double-wave-vector diffusion-weighting experiment to multiple concatenations. J Magn Reson 2009;198:174-182.

36. Finsterbusch J. Numerical simulations of short-mixing-time double-wave-vector diffusion-weighting experiments with multiple concatenations on whole-body MR systems. J Magn Reson 2010;207:274-282.

37. Finsterbusch J. The parallel-antiparallel signal difference in double-wave-vector diffusion-weighted MR at short mixing times: A phase evolution perspective. J Magn Reson 2011;208:114-121.

38. Drobnjak I, Zhang H, Hall MG, and Alexander DC. The matrix formalism for generalised gradients with time-varying orientation in diffusion NMR. J Magn Reson 2011. In Press.

39. Lawrenz M and Finsterbusch J. Detection of microscopic diffusion anisotropy on a whole-body MR system with double wave vector imaging. Magn Reson Med 2011 In Press.

40. Shemesh N, Özarslan E, Komlosh ME, Basser PJ, and Cohen Y. From single-pulsed field gradient to double-pulsed field gradient MR: gleaning new microstructural information and developing new forms of contrast in MRI. NMR Biomed 2010;23:757-780.

41. Finsterbusch J. Multiple-wave-vecto diffusion weighted NMR. Annual Reports NMR Spctrosc. 2011;72:225-299.

42. Paxinos G and Watson C. The rat brain 4th Ed. Academic Press, San Diego 1998.

43. Komlosh ME, Özarslan E, Lizak MJ, Horkay F, Schram V, Shemesh N, Cohen Y, and Basser PJ. Pore diameter mapping using double pulsed-field gradient MRI and its validation using a novel glass capillary array phantom. J Magn Reson 2011;208:128-135.

44. Polleux F, Dehay C, and Kennedy H. The timetable of laminar neurogenesis contributes to the specification of cortical areas in mouse isocortex. J Comp Neurol 1997;385:95-116.

45. Caviness VS, Jr. Architectonic map of neocortex of the normal mouse. J Comp Neurol 1975;164:247-263.

46. Boretius S, Kasper L, Tammer R, Michaelis T, and Frahm J. MRI of cellular layers in mouse brain in vivo. Neuroimage 2009;47:1252-1260.

47. Aoki I, Wu YJL, Silva AC, Lynch RM, and Koretsky AP. In vivo detection of neuroarchitecture in the rodent brain using manganese-enhanced MRI. Neuroimage 2004;22:1046-1059.

48. Beaulieu C. The basis of anisotropic water diffusion in the nervous system - a technical review. NMR Biomed 2002;15:435-455.

49. Lee JH and Springer CS. Effects of equilibrium exchange on diffusion-weighted NMR signals: The diffusigraphic "shutter-speed". Magn Reson Med 2003;49:450-458.

50. Budde MD and Frank JA. Neurite beading is sufficient to decrease the apparent diffusion coefficient after ischemic stroke. Proc Nat Acad Sci USA 2010;107:14472-14477.

Figure Captions

Figure 1. **(A)** The double-Pulsed-Gradient-Spin-Echo (d-PGSE) MRI sequence with EPI readout used in this study. **(B)** The angular d-PFG experiment is performed by keeping the gradient amplitudes constant, while varying the angle ψ between these two gradient vectors. The azimuthal and polar angles in the lab frame, φ_{Lab} and θ_{Lab} are also defined. Note that under these definitions, the rat is aligned with its anterior-posterior axis aligned with the x-axis.

Figure 2. **(A)** The raw $E(\psi)$ data from an angular d-PGSE MRI experiment with EPI readout on an ex-vivo rat brain that was conducted in the X-Y plane (Figure 1). Note the oscillatory signal intensity variance along the different ψ angles. The arrows indicate on areas in the cortex for which the oscillations are visually clear. (B) $E(\psi)_{norm}$ images for the 13 ψ values. After normalizing the data, the oscillations are not influenced by the initial value of $E(\psi=0°)$ in every

voxel, and any bias effects are removed. The oscillations are now purely relative to the ψ=0º image, and their magnitude represents structural parameters as explained in the text.

Figure 3. (A) Regions of interest shown on the ψ=90º d-PGSE MRI images. **(B)** The $E(\psi)_{norm}$ signal oscillations for the three ROIs shown in (A) on the left hemisphere. **(C)** The $E(\psi)_{norm}$ signal oscillations for the three ROIs shown in (A) on the right hemisphere. Three distinct behaviors can be viewed, a nearly perfect oscillation (ROI 1), a phase-shifted oscillation (ROI 2), and an opposite oscillation (ROI 3). **(D)** Twenty four clusters of the pixels in the brain, showing the robust angular patterns in the $E(\psi)_{norm}$ (red asterisks), the fit to Eq. 1 (lines) and the errors (pink asterisks). Eq. 1 describes all clusters adequately, and the errors are close to zero for all clusters. Note that this cluster analysis was only performed to show the robustness of the data, all datasets were eventually analyzed pixel-by-pixel, with no clustering.

Figure 4. (A) A cartoon of a coherently-placed compartment and the orientation of representative gradient pairs in d-PGSE methodology. Here, the first gradient is set in the direction perpendicular to the principal axis of the compartment. At ψ=0º and 180º, free diffusion is measured in both encodings, while at ψ=90º and 270º restricted diffusion is encoded when the second gradient pair is applied. **(B)** The expected $E(\psi)_{norm}$ pattern expected from this experiment. **(C)** A cartoon of a tilted compartment, with the orientation of the same d-PGSE experiment. Note that here, the signal will first decrease owing since less restriction is experienced up to the angle α, creating a phase shift in the data. **(D)** The expected $E(\psi)_{norm}$ pattern expected from this experiment. **(E)** A cartoon of representing an ensemble of tilted compartments that represent a random orientation. The experiment is performed in the X-Y plane. **(F)** The expected $E(\psi)_{norm}$ pattern expected from this experiment. Note that the fractional sum yields the expected angular E(ψ) profile first quantitatively described by the theory in (26).

Figure 5. Analytical curves of $E(\psi)_{norm}$, based on the theory in (26) describing completely randomly oriented cylindrical compartments (red), 30% coherently organized compartments

along θ_{Lab}=90° with φ_{Lab}=45° axis (green) or φ_{Lab}=135° axis (blue) while 70% are completely randomly oriented. Note the phase that emerges in the signal in case of some residual coherence.

Figure 6. (A) Apparent eccentricity (aE) map. **(B)** Absolute valued apparent eccentricity map (|aE|) **(C)** Map of the residual orientation phase φ. **(D)** Maps of the symmetrized phase, φ_{sym}, where the negative colorbar was made equal to the positive colorbar. Note the marked contrast in cortical regions in these images, especially the contrast resembling cortical layering in the aE map and the strong contrast in the medial-lateral direction observed in the φ maps. The experiments were performed in the X-Y plane.

Figure 7. (A-C) Apparent eccentricity (aE), residual phase (φ) and symmetrized residual phase (φ_{sym}) maps for a coronal slice from a different brain and from a more posterior position (compared to Figure 6). **(D-F)** Apparent eccentricity, φ and φ_{sym} maps for an axial slice from yet another different rat brain. These images show the robustness of the analysis across specimens and that imaging gradients do not contribute artifacts owing to cross-terms. Note the abundance of contrast especially in gray matter regions. The experiments were performed in the X-Y plane.

Figure 8. (A) Apparent eccentricity map, **(B)** φ map and **(C)** φ_{sym} map of a coronal slice of the rat brain. **(D)** The anatomical map (42) corresponding to the MRI image. **(E)** Enlargement of the box in (B). The end of the corpus callosum (cc) and the beginning of the cortex are delineated by the dashed line. **(F)** Staining for TH+ neurons. **(G)** Enlargement of the in (F). Note that some residual ordering can be observed.

Figure 9. (A) FA map of an in-vivo rat brain. **(B)** Apparent eccentricity (aE) map of the brain in-vivo. **(C)** A plot of FA or aE values across the line of pixels corresponding to the white lines in (A) and (B), respectively. The pixels are shown from left to right in ascending order. **(D)** Color-coded FA map in the in-vivo brain. **(E)** A map of the residual phase φ from the angular d-PGSE MRI conducted in-vivo. Note that the structural parameters obtained from the d-PGSE MRI offer novel micro-architectural information in-vivo. **(F)** A plot of FA or φ_{sym} values across the line of pixels corresponding to the white lines in (D) and (E), respectively. The pixels are shown from

left to right in ascending order. Note the new contrasts that are observed in the cortex in-vivo using d-PGSE MRI.

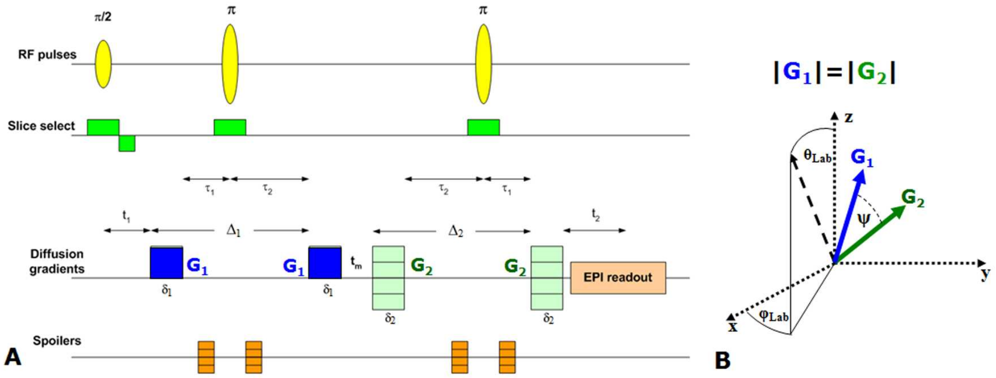

Figure 1. (A) The double-Pulsed-Gradient-Spin-Echo (d-PGSE) MRI sequence with EPI readout used in this study. (B) The angular d-PFG experiment is performed by keeping the gradient amplitudes constant, while varying the angle ψ between these two gradient vectors. The azimuthal and polar angles in the lab frame, φLab and θLab are also defined. Note that under these definitions, the rat is aligned with its anterior-posterior axis aligned with the x-axis.

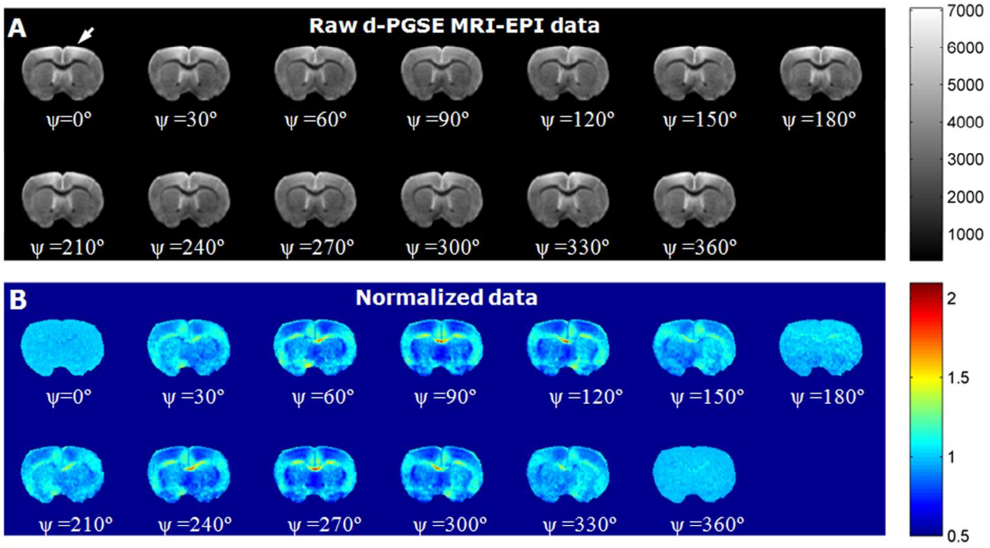

Figure 2. (A) The raw $E(\psi)$ data from an angular d-PGSE MRI experiment with EPI readout on an ex-vivo rat brain that was conducted in the X-Y plane (Figure 1). Note the oscillatory signal intensity variance along the different ψ angles. The arrows indicate on areas in the cortex for which the oscillations are visually clear. (B) $E(\psi)$norm images for the 13 ψ values. After normalizing the data, the oscillations are not influenced by the initial value of $E(\psi=0^{\circ})$ in every voxel, and any bias effects are removed. The oscillations are now purely relative to the $\psi=0^{\circ}$ image, and their magnitude represents structural parameters as explained in the text.

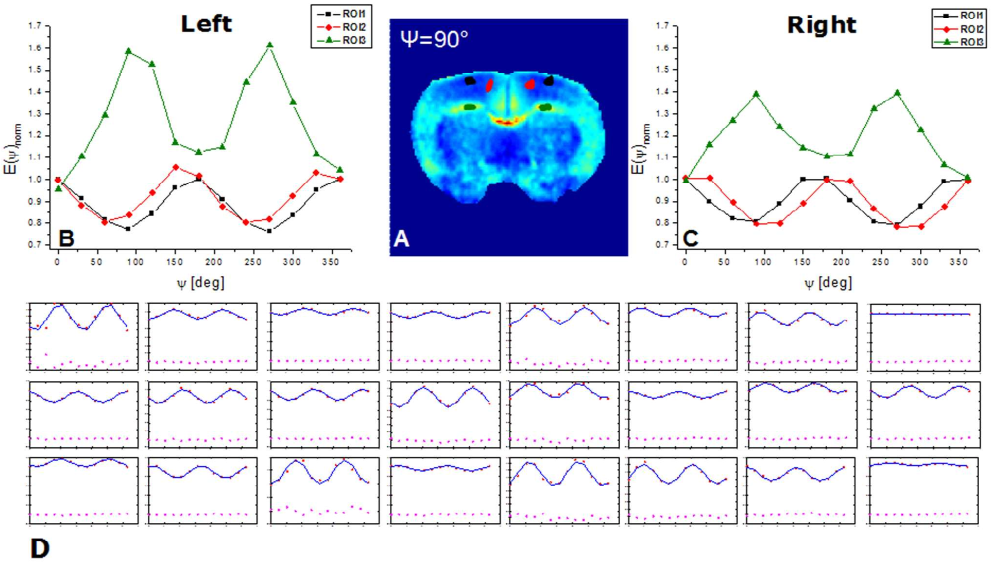

Figure 3. (A) Regions of interest shown on the ψ=90º d-PGSE MRI images. (B) The E(ψ)norm signal oscillations for the three ROIs shown in (A) on the left hemisphere. (C) The E(ψ)norm signal oscillations for the three ROIs shown in (A) on the right hemisphere. Three distinct behaviors can be viewed, a nearly perfect oscillation (ROI 1), a phase-shifted oscillation (ROI 2), and an opposite oscillation (ROI 3). (D) Twenty four clusters of the pixels in the brain, showing the robust angular patterns in the E(ψ)norm (red asterisks), the fit to Eq. 1 (lines) and the errors (pink asterisks). Eq. 1 describes all clusters adequately, and the errors are close to zero for all clusters. Note that this cluster analysis was only performed to show the robustness of the data, all datasets were eventually analyzed pixel-by-pixel, with no clustering.

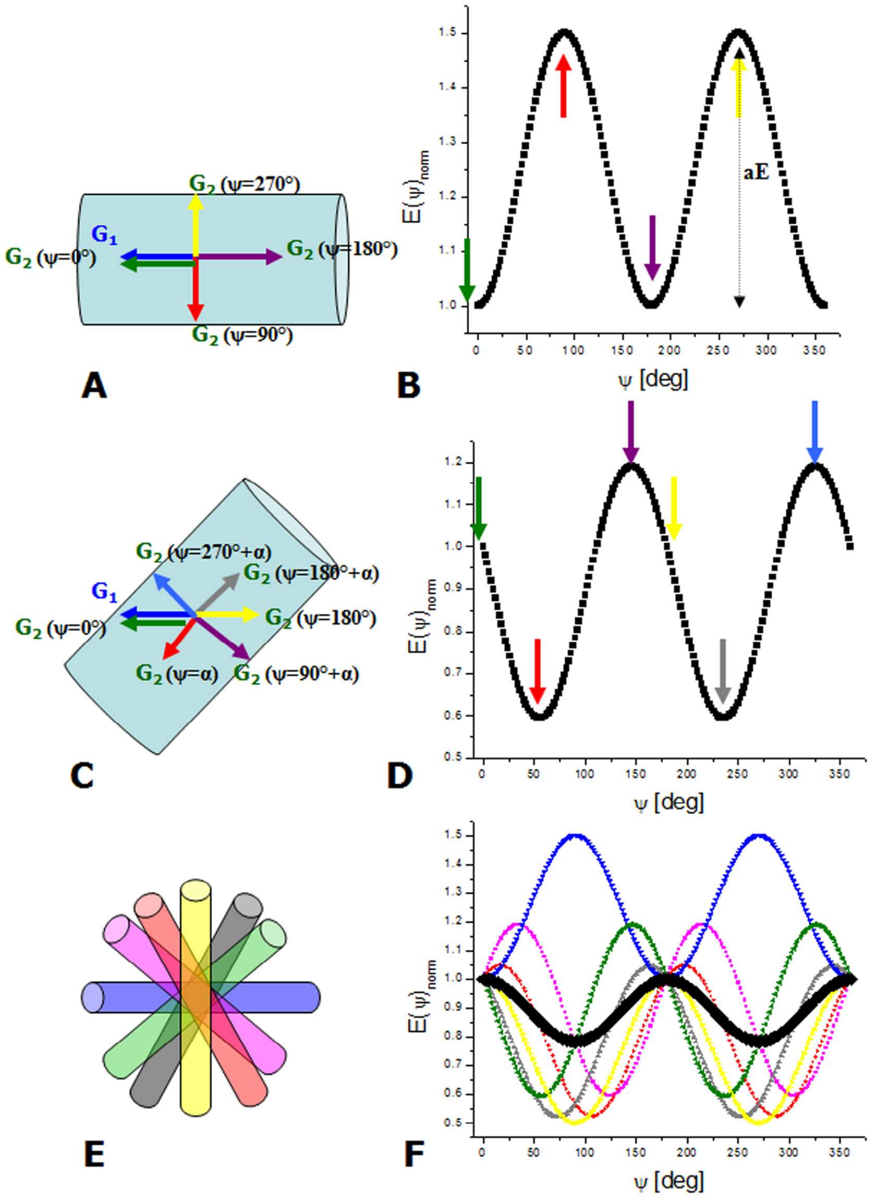

Figure 4. (A) A cartoon of a coherently-placed compartment and the orientation of representative gradient pairs in d-PGSE methodology. Here, the first gradient is set in the direction perpendicular to the principal axis of the compartment. At ψ=0º and 180º, free diffusion is measured in both encodings, while at ψ=90º and 270º restricted diffusion is encoded when the second gradient pair is applied. (B) The expected E(ψ)norm pattern expected from this experiment. (C) A cartoon of a tilted compartment, with the orientation of the same d-PGSE experiment. Note that here, the signal will first decrease owing since less restriction is experienced up to the angle ɑ, creating a phase shift in the data. (D) The expected E(ψ)norm pattern expected from this experiment. (E) A cartoon of representing an ensemble of tilted compartments that represent a random orientation. The experiment is performed in the X-Y plane. (F) The expected E(ψ)norm pattern expected from this experiment. Note that the fractional sum yields the expected angular E(ψ) profile first quantitatively described by the theory in (26).

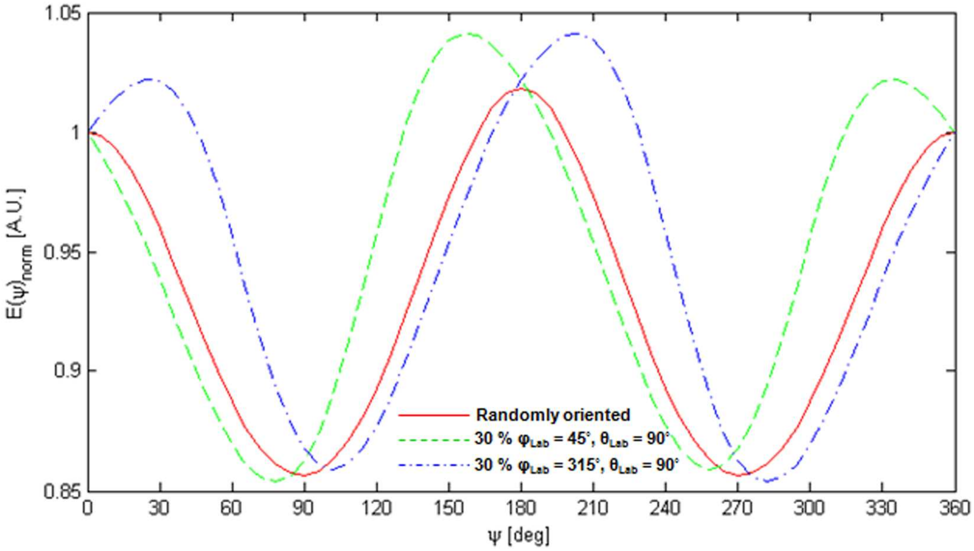

Figure 5. Analytical curves of E(ψ)norm, based on the theory in (26) describing completely randomly oriented cylindrical compartments (red), 30% coherently organized compartments along θLab=90º with φLab=45º axis (green) or φLab=135º axis (blue) while 70% are completely randomly oriented. Note the phase that emerges in the signal in case of some residual coherence.

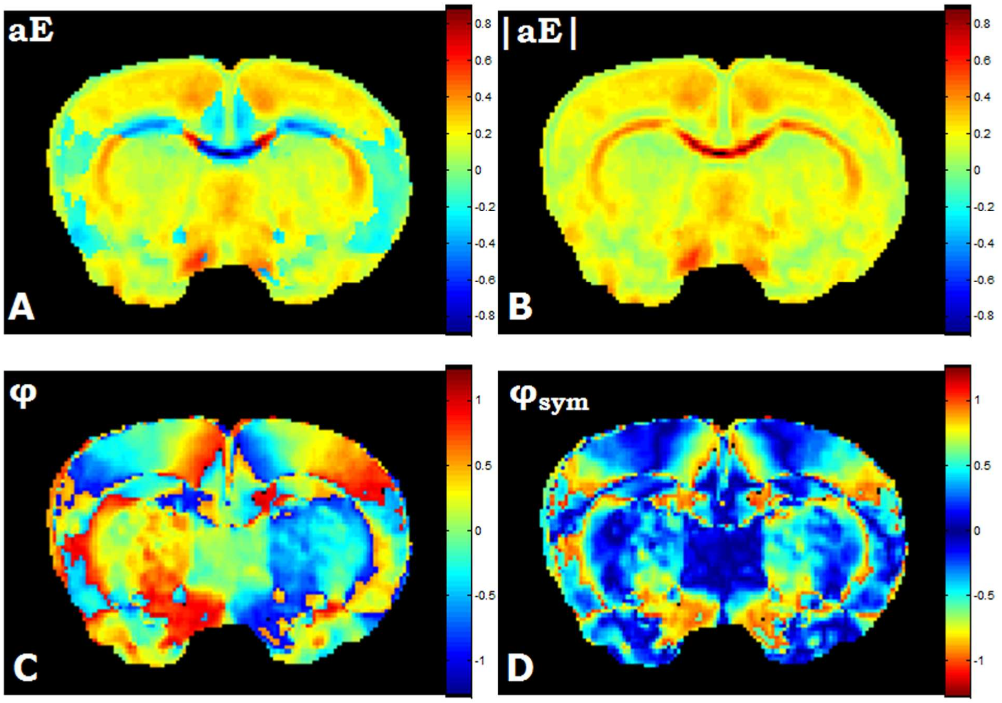

Figure 6. (A) Apparent eccentricity (aE) map. (B) Absolute valued apparent eccentricity map (|aE|) (C) Map of the residual orientation phase φ. (D) Maps of the symmetrized phase, φsym, where the negative colorbar was made equal to the positive colorbar. Note the marked contrast in cortical regions in these images, especially the contrast resembling cortical layering in the aE map and the strong contrast in the medial-lateral direction observed in the φ maps. The experiments were performed in the X-Y plane.

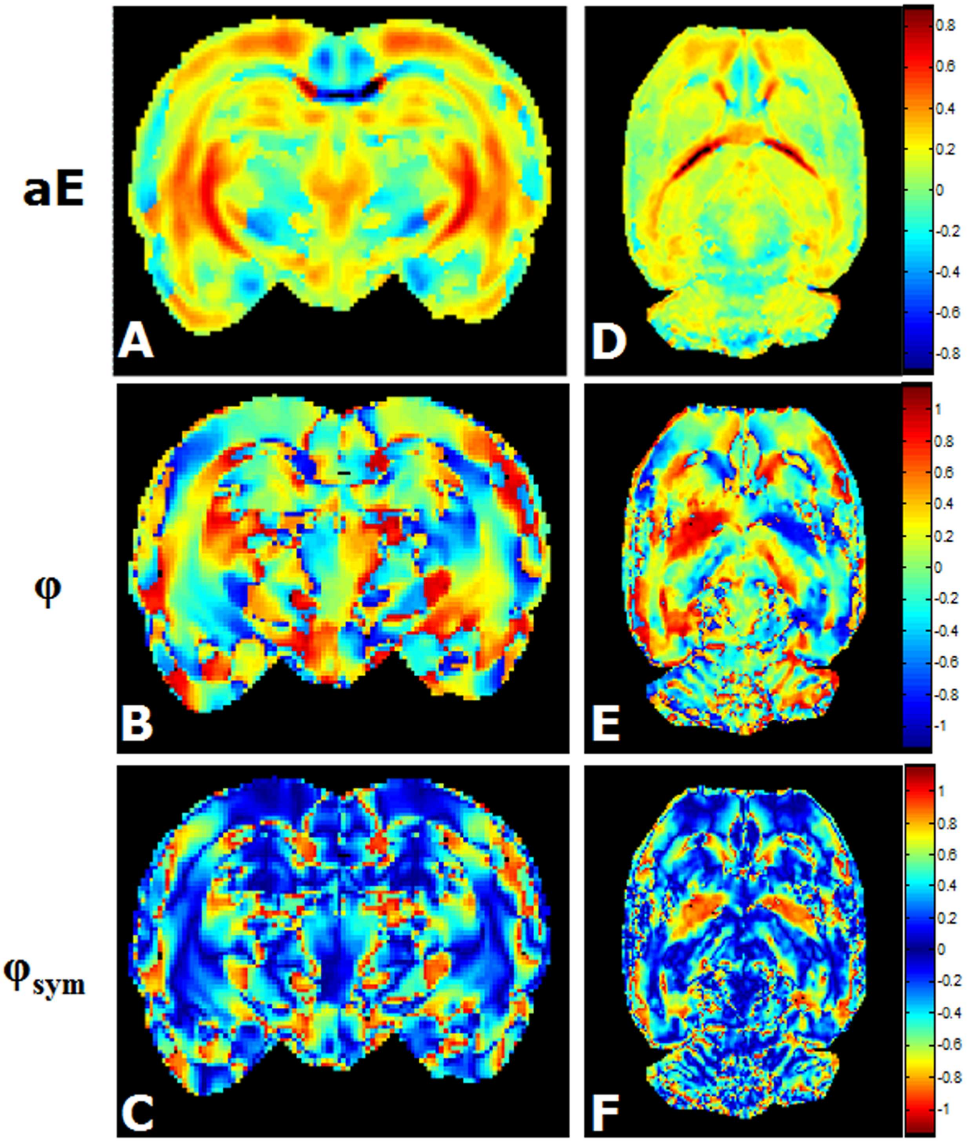

Figure 7. (A-C) Apparent eccentricity (aE), residual phase (φ) and symmetrized residual phase (φsym) maps for a coronal slice from a different brain and from a more posterior position (compared to Figure 6). (D-F) Apparent eccentricity, φ and φsym maps for an axial slice from yet another different rat brain. These images show the robustness of the analysis across specimens and that imaging gradients do not contribute artifacts owing to cross-terms. Note the abundance of contrast especially in gray matter regions. The experiments were performed in the X-Y plane.

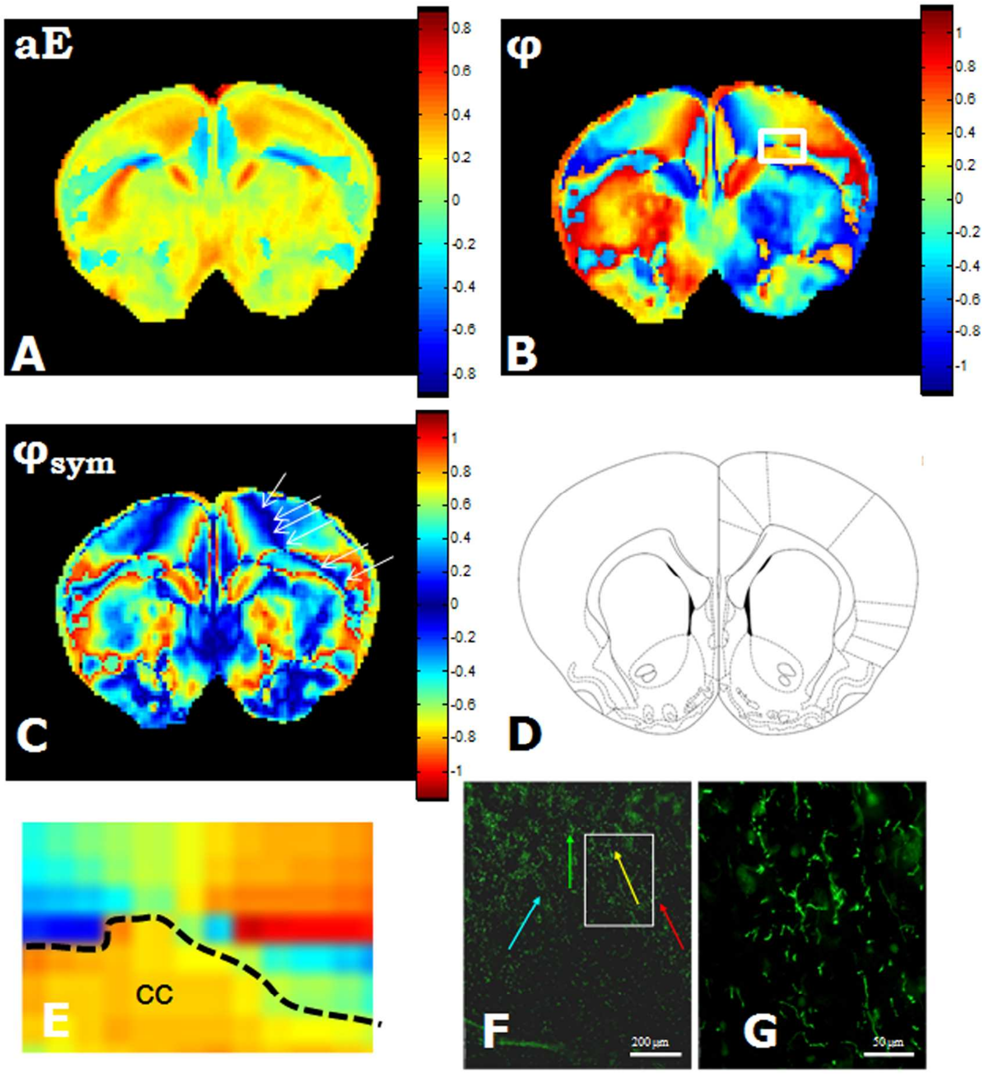

Figure 8. (A) Apparent eccentricity map, (B) φ map and (C) φsym map of a coronal slice of the rat brain. (D) The anatomical map (42) corresponding to the MRI image. (E) Enlargement of the box in (B). The end of the corpus callosum (cc) and the beginning of the cortex are delineated by the dashed line. (F) Staining for TH+ neurons. (G) Enlargement of the in (F). Note that some residual ordering can be observed.

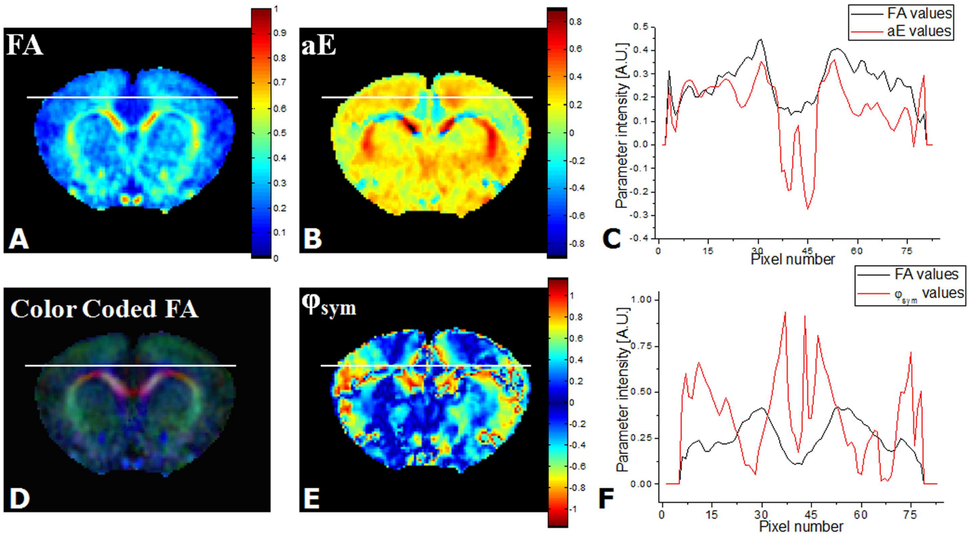

Figure 9. (A) FA map of an in-vivo rat brain. (B) Apparent eccentricity (aE) map of the brain in-vivo. (C) A plot of FA or aE values across the line of pixels corresponding to the white lines in (A) and (B), respectively. The pixels are shown from left to right in ascending order. (D) Color-coded FA map in the in-vivo brain. (E) A map of the residual phase φ from the angular d-PGSE MRI conducted in-vivo. Note that the structural parameters obtained from the d-PGSE MRI offer novel micro-architectural information in-vivo. (F) A plot of FA or φsym values across the line of pixels corresponding to the white lines in (D) and (E), respectively. The pixels are shown from left to right in ascending order. Note the new contrasts that are observed in the cortex in-vivo using d-PGSE MRI.